Petroleum Science 21 (2024) 4052–4066

Contents lists available at ScienceDirect

Petroleum Science

journal homepage: www.keaipublishing.com/en/journals/petroleum-science

Original Paper

Extraction of ADCIGs in viscoelastic media based on fractional viscoelastic equations

Wen-Bin Tian [a, b], Yang Liu [a, b, c, *], Jiang-Tao Ma [a, b]

[a] National Key Laboratory of Petroleum Resources and Engineering, China University of Petroleum (Beijing), Beijing, 102249, China
[b] College of Geophysics, China University of Petroleum (Beijing), Beijing 102249, China
[c] College of Petroleum, China University of Petroleum (Beijing), Karamay Campus, Karamay, 834000, Xinjiang, China

A R T I C L E I N F O

Article history:
Received 24 January 2024
Received in revised form
21 July 2024
Accepted 30 September 2024
Available online 2 October 2024

Edited by Meng-Jiao Zhou and Min Li

Keywords:
Viscoelastic media
Fractional viscoelastic equations
Angle domain common imaging gathers (ADCIGs)
Attenuation effects

A B S T R A C T

Angle domain common imaging gathers (ADCIGs) serve as not only an ideal approach for tomographic velocity modeling but also as a crucial means of mitigating low-frequency noise. Thus, they play a significant role in seismic data processing. Recently, the Poynting vector method, due to its lower computational requirements and higher resolution, has become a commonly used approach for obtaining ADCIGs. However, due to the viscoelastic properties of underground media, attenuation effects (phase dispersion and amplitude attenuation) have become a factor, which is important in seismic data processing. However, the primary applications of ADCIGs are currently confined to acoustic and elastic media. To assess the influence of attenuation and elastic effects on ADCIGs, we introduce an extraction method for ADCIGs based on fractional viscoelastic equations. This method enhances ADCIGs accuracy by simultaneously considering both the attenuation and elastic properties of underground media. Meanwhile, the S-wave quasi tensor is used to reduce the impact of P-wave energy on S-wave stress, thus further increasing the accuracy of PS-ADCIGs. In conclusion, our analysis examines the impact of the quality factor Q on ADCIGs and offers theoretical guidance for parameter inversion.

1. Introduction

Common imaging gathers (CIGs), which are intermediate data obtained from pre-stack migration imaging methods, encapsulate crucial information about the velocity and lithology of underground media (Zhang and McMechan, 2011a, 2010). This establishes CIGs as powerful tools in both migration velocity analysis (MVA) (Biondi and Tisserant, 2004) and amplitude variation with angle/offset (AVA/AVO) (Canning and Malkin, 2009). Commonly utilized CIGs primarily comprise offset domain common imaging gathers (ODCIGs) and angle domain common imaging gathers (ADCIGs). However, ODCIGs encounter limitations in MVA, AVA and AVO analyses due to the prevalence of offset artifacts arising from the multipath problem. ADCIGs are adept at effectively addressing this issue, thereby offering more prospects for development (Mosher et al., 1997). Simultaneously, given the widespread viscoelastic properties of underground media, the extraction of ADCIGs based on viscoelastic models has attracted considerable attention.

Currently, ADCIGs can be acquired using various methods, including Kirchhoff migration, one-way wave migration and two-way wave migration (Sava and Fomel, 2003; Biondi, 2007; Liu et al., 2015). Here, our focus is on extracting angle gathers using two-way wave migration, specifically reverse time migration (RTM). Three ways are often used to produce ADCIGs for RTM. Presently, there are three prevalent methods used for obtaining ADCIGs based on RTM. One of the methods for extracting ADCIGs is through an indirect approach, like the extended imaging condition approach (Sava and Biondi, 2004; Biondi and Symes, 2004). In this method, ODCIGs are initially generated using a local-shift extended imaging condition. Subsequently, these ODCIGs are converted into ADCIGs through either Fourier transform or slant stack transform. The other method is a direct method called local plane-wave decomposition (LPWD) method (Soubaras, 2003; Xu et al., 2011; Tang and McMechan, 2016). This method adopts the LPWD method to decompose the source and receiver wavefields into local angle components, and then uses angle domain cross-correlation imaging conditions to output ADCIGs. However, both methods mentioned earlier face significant challenges in terms of

* Corresponding author. National Key Laboratory of Petroleum Resources and Engineering, China University of Petroleum (Beijing), Beijing, 102249, China.
E-mail address: wliuyang@vip.sina.com (Y. Liu).

https://doi.org/10.1016/j.petsci.2024.09.027

computational cost, which can be a limiting factor in practical applications. The last method for extracting ADCIGs is based on direction vector methods, including Poynting vector-based method (Yoon et al., 2011; McGarry and Qin, 2013; Tang et al., 2017), the polarization-based method (Zhang and McMechan, 2013) and optical-flow-based method (Gong et al., 2016). These methods directly extract ADCIGs during reverse time migration, offering a cost-effective approach for obtaining ADCIGs. This final method has garnered increased attention from scholars due to its significant advantages (Yang et al., 2016, 2022; Hu et al., 2019; Li et al., 2021). ADCIGs have become a versatile tool in the wavefield of seismic data analysis. They are not only used for tomographic velocity inversion through residual velocity analysis (Koren et al., 2008; Zhou et al., 2011), but also play a crucial role in noise suppression during migration through angle-based stacking techniques (Jin et al., 2015). However, the extraction of ADCIGs has been primarily focused on acoustic media (Jin et al., 2014; Hu et al., 2016), elastic wave media (Liu, 2019) and anisotropic media (Alkhalifah and Fomel, 2009). The focus of this paper is to extend the extraction of ADCIGs to viscoelastic media, which is an important and challenging area of study in the wavefield of seismic imaging and analysis.

As exploration targets become more complex, it becomes crucial to account for the impact of attenuation and elasticity in the media (Robertsson et al., 1994). A considerable number of scholars have made significant contributions to advancing modeling and migration methods in viscoelastic media. Currently, two widely adopted methods for simulating the propagation of seismic waves in viscoelastic media are the standard linear solids (SLS) model and the decoupled fractional Laplacian (DFL) approach (Chen et al., 2023). The viscoelastic equations based on the SLS model can be efficiently solved using finite difference methods. However, incorporating the SLS model into these equations adds to the complexity of the wave equations (Hu et al., 2019). Simultaneously, using the SLS-based model to effectively correct phase distortion and counteract energy loss is a substantial challenge (Chen and Holm, 2004). The DFL-based method can overcome this problem due to its two fractional Laplace operators, which are specifically designed to manage amplitude attenuation and phase distortion, respectively (Zhu and Harris, 2014; Zhu and Carcione, 2014; Chen et al., 2016). The DFL-based method has been adapted for use in viscoelastic media, allowing for the acquisition of multi-component seismic data (Zhu, 2017a; Moradi and Innanen, 2017; Wang et al., 2018a). The fractional operator, varying with the quality factor and changing across locations, is difficult to solve using traditional finite difference (FD) methods (Carcione et al., 2002). To overcome this difficulty, the optimal staggered grid finite-difference method based on binomial windows (Sun et al., 2017) and the local finite-difference approach (Song et al., 2020) have been proposed as solutions for the fractional wave equation. Additionally, to efficiently address fractional order operators in DFL-based methods, several techniques have been introduced. These techniques include low-rank decomposition, Taylor series expansion, and the utilization of partial independent fractional operators (Sun et al., 2015; Guo et al., 2016; Chen et al., 2019; Xing and Zhu, 2019; Zhang et al., 2020). The DFL-based method possesses the inherent capability to recover amplitude attenuation and handle phase dispersion. Through altering the sign of the amplitude dissipation term, it accomplishes Q-compensated RTM (QRTM), thereby ensuring the preservation of phase dispersion and amplitude attenuation during both forward and backward wave propagation (Zhu et al., 2014). The DFL-based method, serving as a compelling solution for QRTM, forms the foundation of our research.

Viscoelastic reverse time migration (QERTM), which employs the vector viscoelastic wave equation, offers the advantage of producing multi-wave imaging for a more comprehensive understanding of subsurface structures. Additionally, it addresses the issue of inaccurate imaging caused by seismic wave absorption attenuation (Chang and McMechan, 1987; Yoon et al., 2004; Deng and McMechan, 2008; Li et al., 2016a). In QERTM, a multi-wave imaging method, the separation of P-waves and S-waves is achieved by means of Helmholtz decomposition and the decoupling equations. This process helps to effectively reduce crosstalk noise, allowing for clearer imaging of subsurface structures (Sun et al., 2004; Du et al., 2017). In the Helmholtz decomposition method, which is widely used in QERTM, the S-wave is obtained by performing a curl operation on the wavefield, while the P-wave is derived through a divergence operation. This separation of P-waves and S-waves is crucial for accurate imaging in viscoelastic media (Zhang et al., 2010; Li et al., 2016b; Zhu, 2017b). However, while the Helmholtz decomposition method effectively separates P-waves and S-waves, the resulting wavefield may exhibit amplitude and phase distortions. These distortions can affect the accuracy of imaging in viscoelastic media (Du et al., 2012). On the other hand, the decoupling equation method directly extracts separated P-waves and S-waves as the wavefield propagates, bypassing the need for post-processing operations like curl and divergence operations. This method can help reduce amplitude and phase distortion in the separated wavefields (Xiao and Leaney, 2010; Wang et al., 2015). Furthermore, it's worth noting that the energy compensation process in RTM based on viscoelastic (QERTM) and viscoacoustic media (QRTM), characterized by exponential amplification, can be susceptible to instability during the compensation phase. This instability can pose challenges when applying compensation techniques in such media (Zhao et al., 2018; Wang et al., 2022). To solve this issue, one effective solution is to apply a low-pass filter. This filter can help stabilize the compensation process and mitigate the instability associated with exponential amplification in QERTM and QRTM. However, using a low-pass filter in RTM to stabilize compensation in QERTM and QRTM filters out high-frequency noise but may also lead to the loss of important seismic signals (Sun and Zhu, 2018). To preserve important seismic signals while stabilizing compensation in viscoelastic and viscoacoustic media, several compensation operators have been proposed, yielding positive application outcomes (Xie et al., 2015; Wang et al., 2017a, 2017b, 2018a, 2019). Currently, there is limited research focused on extracting ADCIGs based on viscoelastic media.

Expanding on the stable framework of QERTM, we have extended the method to extract ADCIGs within viscoelastic media. This novel method, based on viscoelastic media that consider both attenuation and elasticity, not only enhances the accuracy of ADCIGs but also compensates for the energy of deep ADCIGs. This represents a significant advancement compared to traditional methods based on elastic media. Specifically, we implement PP and PS imaging based on decoupled viscoelastic equations. During the imaging process, we simultaneously extract the ADCIGs for PP-images and PS-images using the Poynting Vector method. Furthermore, we enhance the accuracy of the S-wave Poynting vector by utilizing the S-wave quasi-tensor. Finally, we conduct separate analyses on the effects of the quality factor Q on P-waves and S-waves in ADCIGs, providing valuable insights for tomographic inversion.

2. Theory and method

In this section, we will first introduce a method for implementing QERTM using decoupling equations. Next, we will explain how to calculate the Poynting vector. Finally, building upon these foundations, we will present a method for extracting ADCIGs in viscoelastic media.

2.1. The review of reverse time migration based on viscoelastic media

In QERTM, the viscoelastic extrapolation method couples not only P-wave and S-wave components but is also influenced by seismic attenuation and dispersion effects. Therefore, to achieve viscoelastic imaging, it is necessary to implement wavefield simulation, wavefield decomposition and attenuation compensation.

2.1.1. Viscoelastic wave equation

The 2D DFL viscoelastic wave equation offers a notable advantage due to its ability to decouple correlation terms of amplitude attenuation and phase distortion. This unique feature allows for a more accurate simulation of seismic wave propagation in viscoelastic media. The specific equation (Zhu and Harris, 2014) is as follows:

$$\begin{cases} \dfrac{\partial v_x}{\partial t} = \dfrac{1}{\rho}\dfrac{\partial \tau_{xx}}{\partial x} + \dfrac{1}{\rho}\dfrac{\partial \tau_{xz}}{\partial z} \\ \dfrac{\partial v_z}{\partial t} = \dfrac{1}{\rho}\dfrac{\partial \tau_{xz}}{\partial x} + \dfrac{1}{\rho}\dfrac{\partial \tau_{zz}}{\partial z} \\ \dfrac{\partial \tau_{xx}}{\partial t} = D_p\dfrac{\partial v_x}{\partial x} + D_p\dfrac{\partial v_z}{\partial z} - 2D_s\dfrac{\partial v_z}{\partial z} \\ \dfrac{\partial \tau_{zz}}{\partial t} = D_p\dfrac{\partial v_x}{\partial x} - 2D_s\dfrac{\partial v_x}{\partial x} + D_p\dfrac{\partial v_z}{\partial z} \\ \dfrac{\partial \tau_{xz}}{\partial t} = D_s\dfrac{\partial v_z}{\partial x} + D_s\dfrac{\partial v_x}{\partial z} \end{cases}, \tag{1}$$

where $v = (v_x, v_z)$ and $\tau = (\tau_{xx}, \tau_{zx}, \tau_{zz})$ are particle velocity and stress components separately; ρ represents the density; $D = (D_p, D_s)$ are functions related to velocity $V = (V_p, V_s)$ and quality factors $Q = (Q_p, Q_s)$ of the P-wave and S-wave, and they can be described as:

$$D_\varsigma(t) \approx a\left(-\nabla^2\right)^{\gamma_\varsigma} + b\left(-\nabla^2\right)^{\gamma_\varsigma - 0.5}\partial_t, \tag{2}$$

where ς represents the parameters related to P-wave and S-wave, respectively; $(-\nabla^2)^{\gamma_\varsigma}$ and $(-\nabla^2)^{\gamma_\varsigma-0.5}$ are two fractional Laplacian operators, which the first specifically solves seismic wave attenuation, and the second effectively manages phase dispersion effects; $\gamma_\varsigma = \arctan(1/Q_\varsigma)/\pi$ is the fractional order associated with the quality factor Q_ς of P-wave and S-wave. The intermediate variable a and b in Eq. (2) can be defined as:

$$\begin{cases} a = M(V_\varsigma/\omega_0)^{2\gamma_\varsigma}\cos(\pi\gamma_\varsigma) \\ b = M(V_\varsigma/\omega_0)^{2\gamma_\varsigma-1}\omega_0^{-1}\sin(\pi\gamma_\varsigma) \\ M = \rho V_\varsigma^2\cos^2\left(\dfrac{\pi\gamma_\varsigma}{2}\right) \end{cases}, \tag{3}$$

where $\omega_0 = 2\pi f_0$ represents the reference angular frequency, V_ς is the reference velocity of P-wave and S-wave. In this study, we utilize the staged grid pseudo spectral (SGPS) method to solve the DFL viscoelastic equation.

2.1.2. The decoupled viscoelastic wave equation

QERTM utilizes the viscoelastic wave equation for wavefield extension and applies wavefield separation techniques to distinctly isolate P-wave and S-wave wavefields, enabling more detailed analysis. Subsequently, applying elastic wave imaging conditions, it successfully obtains the final PP-wave and PS-wave migration image. The decoupled P-wave viscoelastic equation (Xiao and Leaney, 2010; Wang et al., 2015) can be described as follows:

$$\begin{cases} \dfrac{\partial v_{xp}}{\partial t} = \dfrac{1}{\rho}\dfrac{\partial \tau_p}{\partial x} \\ \dfrac{\partial v_{zp}}{\partial t} = \dfrac{1}{\rho}\dfrac{\partial \tau_p}{\partial z} \\ \dfrac{\partial \tau_p}{\partial t} = D_p\left(\dfrac{\partial v_x}{\partial x} + \dfrac{\partial v_z}{\partial z}\right) \end{cases}, \tag{4}$$

where $v_p = (v_{xp}, v_{zp})$ is the particle velocity of P-wave; τ_p represents the stress component of P-wave, which is a scalar quantity; The particle velocity of S-wave $v_s = (v_{xs}, v_{zs})$ can be obtained as follows:

$$\begin{cases} v_{xs} = v_x - v_{xp} \\ v_{zs} = v_z - v_{zp} \end{cases}. \tag{5}$$

In QERTM, with $v_p = (v_{xp}, v_{zp})$ and $v_s = (v_{xs}, v_{zs})$, we can obtain PP-image (I_{pp}) and PS-image (I_{ps}) with inner product conditions (Du et al., 2012):

$$\begin{cases} I_{pp} = \dfrac{\int_0^T v_p^{\mathrm{Sou}}(t)\cdot v_p^{\mathrm{Rec}}(t)}{\int_0^T v_p^{\mathrm{Sou}}(t)\cdot v_p^{\mathrm{Sou}}(t)}\mathrm{d}t \\ I_{ps} = \dfrac{\int_0^T v_p^{\mathrm{Sou}}(t)\cdot v_s^{\mathrm{Rec}}(t)}{\int_0^T v_p^{\mathrm{Sou}}(t)\cdot v_p^{\mathrm{Sou}}(t)}\mathrm{d}t \end{cases}, \tag{6}$$

where superscripts Sou and Rec denote the source and receiver wavefields, respectively. However, to calculate the Poynting vector, the stress components of both P-wave and S-wave are required. In the traditional method, the stress component of the S-wave is subtracted from the total stress component, the stress components ($\tau_S(t_{xxs}, t_{zzs}, t_{xzs})$) of S-wave can be obtained:

$$\begin{cases} \dfrac{\partial \tau_{xxs}}{\partial t} = -2D_s\dfrac{\partial v_z}{\partial z} \\ \dfrac{\partial \tau_{zzs}}{\partial t} = -2D_s\dfrac{\partial v_x}{\partial x} \\ \dfrac{\partial \tau_{xzs}}{\partial t} = D_s\left(\dfrac{\partial v_x}{\partial z} + \dfrac{\partial v_z}{\partial x}\right) \end{cases}. \tag{7}$$

Due to P-wave stress crosstalk in the stress component derived from Eq. (7), we utilize the S-wave quasi tensor to calculate the S-wave stress, which can be expressed as follows:

$$\begin{cases} \dfrac{\partial \tau_{xxs}}{\partial t} = -2D_s\dfrac{\partial v_{zs}}{\partial z} \\ \dfrac{\partial \tau_{zzs}}{\partial t} = -2D_s\dfrac{\partial v_{xs}}{\partial x} \\ \dfrac{\partial \tau_{xzs}}{\partial t} = D_s\left(\dfrac{\partial v_{xs}}{\partial z} + \dfrac{\partial v_{zs}}{\partial x}\right) \end{cases}. \tag{8}$$

Applying Eqs. (1), (4), (5) and (8), we can determine the particle velocity and stress components of both P-waves and S-waves, which are essential for extracting ADCIGs. As the attenuation medium is a time-varying system marked by an exponential decrease in seismic wave energy, the energy compensation required for attenuation also increases exponentially with propagation time. This increase is related to the wavenumber, suggesting that components with high wavenumbers may cause instability during the compensation process. In this paper, we use adaptive stability for

Q-ERTM (Appendix A).

2.2. Extracting ADCIGs of PP and PS based on poynting vectors

The Poynting vector is originally used to represent the direction of electromagnetic wave propagation. Subsequently, it is introduced into seismic exploration as a basis for an imaging condition. In seismology, the Poynting vector (*Poynting*) (Yoon and Marfurt, 2006) is expressed as follows:

$$Poynting = -v \cdot \tau, \tag{9}$$

where v and τ represent particle velocity and stress components respectively. Since these variables are already calculated during the RTM process, computing the Poynting vector becomes cost-effective. In viscoelastic media, the Poynting vector for P-waves ($Poynting_j^p$) can be represented as follows:

$$Poynting_j^p = -\tau_p v_{jp}, \tag{10}$$

Correspondingly, the Poynting vector of the S-wave ($Poynting_j^s$) is obtained as follows:

$$Poynting_j^s = -\tau_{jks} v_{ks}, \tag{11}$$

where j and k stand for the x and z components respectively; s and p respectively represent parameters associated with the P-wave and the S-wave. After calculating the Poynting vectors of the source wavefield (S^p_{Poynting}) and the receive wavefield (R^p_{Poynting}) separately, we can obtain the cosine of the angle (φ_{pp}) between them using the following equation:

$$\cos \varphi_{pp} = \frac{S^p_{\text{Poynting}} R^p_{\text{Poynting}}}{\left|S^p_{\text{Poynting}} R^p_{\text{Poynting}}\right|}. \tag{12}$$

Referring to Fig. 1, the incident angle of P-wave (θ_p) can be calculated based on this angle (φ_{pp}). This calculation formula can be expressed as follows:

$$\theta_p = \frac{1}{2} \arccos \varphi_{pp}. \tag{13}$$

However, considering the disparity in velocities between P-waves and S-waves, we can determine the reflection angle of S-wave (θ_s) waves using Snell's law:

$$\sin \theta_p / V_p = \sin \theta_s / V_s. \tag{14}$$

To simplify the calculation, the S-wave reflection angle can be obtained based on the triangle area (Liu et al., 2017), as described below:

$$\theta_s = \arcsin \frac{V_s \sin \varphi_{ps}}{\sqrt{V_p^2 + V_s^2 + 2V_p V_s \cos \varphi_{ps}}}, \tag{15}$$

where $\varphi_{ps} = \theta_s + \theta_p$ can be calculated as follows:

$$\varphi_{ps} = \frac{1}{2} \arccos \frac{S^p_{\text{Poynting}} R^s_{\text{Poynting}}}{\left|S^p_{\text{Poynting}} R^s_{\text{Poynting}}\right|}. \tag{16}$$

After obtaining the P-wave incidence angle θ_p and the S-wave reflection angle θ_s, we can obtain the PP-ADCIGs ($ADCIGs_{pp}$) and PS-ADCIGs ($ADCIGs_{ps}$). This process (Wang et al., 2013) can be expressed as follows:

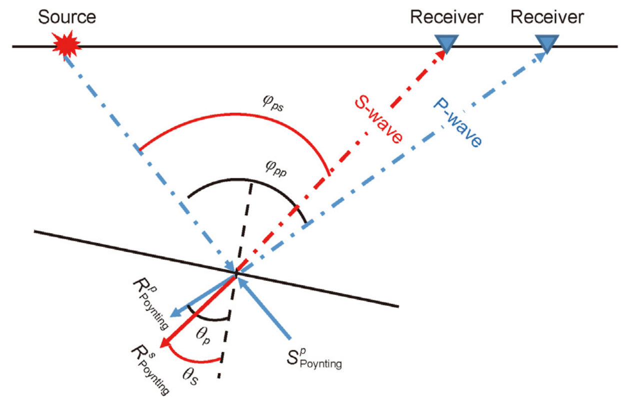

Fig. 1. Schematic diagram of calculating the incident angle (θ_p) of P-wave and reflection angle (θ_s) of S-wave using Poynting vectors.

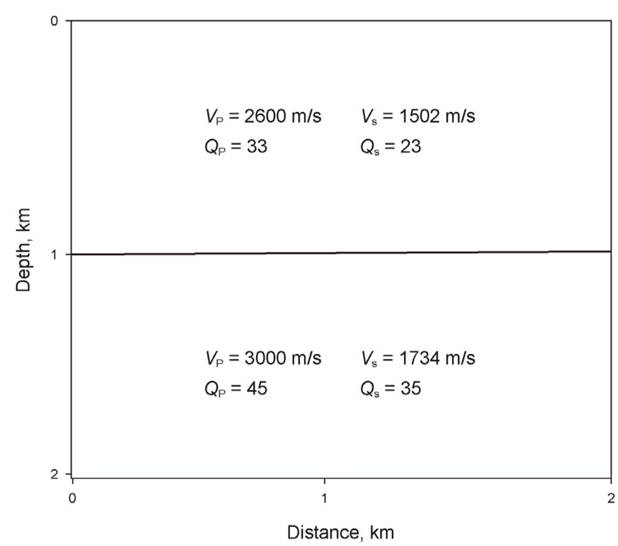

Fig. 2. Viscoelastic parameters of the layer model.

$$\begin{cases} ADCIGs_{pp}(x,\beta_k) = \sum\limits_{i_s}^{\text{ns}} \dfrac{\sum\limits_{t=0}^{T_{\max}} v_p^{\text{sou}}(t,x) \cdot v_p^{\text{rec}}(t,x) \exp\left[-\dfrac{(\theta_p - \beta_k)^2}{2\sigma^2}\right]}{\sum\limits_{t=0}^{T_{\max}} v_P^{\text{sou}}(t,x) \cdot v_P^{\text{sou}}(t,x)} \\ ADCIGs_{ps}(x,\beta_k) = \sum\limits_{i_s}^{\text{ns}} \dfrac{\sum\limits_{t=0}^{T_{\max}} v_p^{\text{sou}}(t,x) \cdot v_s^{\text{rec}}(t,x) \exp\left[-\dfrac{(\theta_s - \beta_k)^2}{2\sigma^2}\right]}{\sum\limits_{t=0}^{T_{\max}} v_P^{\text{sou}}(t,x) \cdot v_P^{\text{sou}}(t,x)} \end{cases}, \tag{17}$$

where β_k is the k_{th} discrete angle; x, t and i_s stand for the imaging point at the S_{th} and image time, respectively; $T_{\max}$ and ns represent the maximum recording time and number of shots; v_s^{rec} and v_p^{rec} are the P-wave and S-wave particle velocity obtained from receivers; v_p^{sou} stands for the P-wave particle velocity obtained from sources; σ represents the variance of the Gaussian function. To enhance the signal-to-noise ratio of ADCIGs and ensure the in-phase axes of these gathers clearer and more continuous, we employ triangle

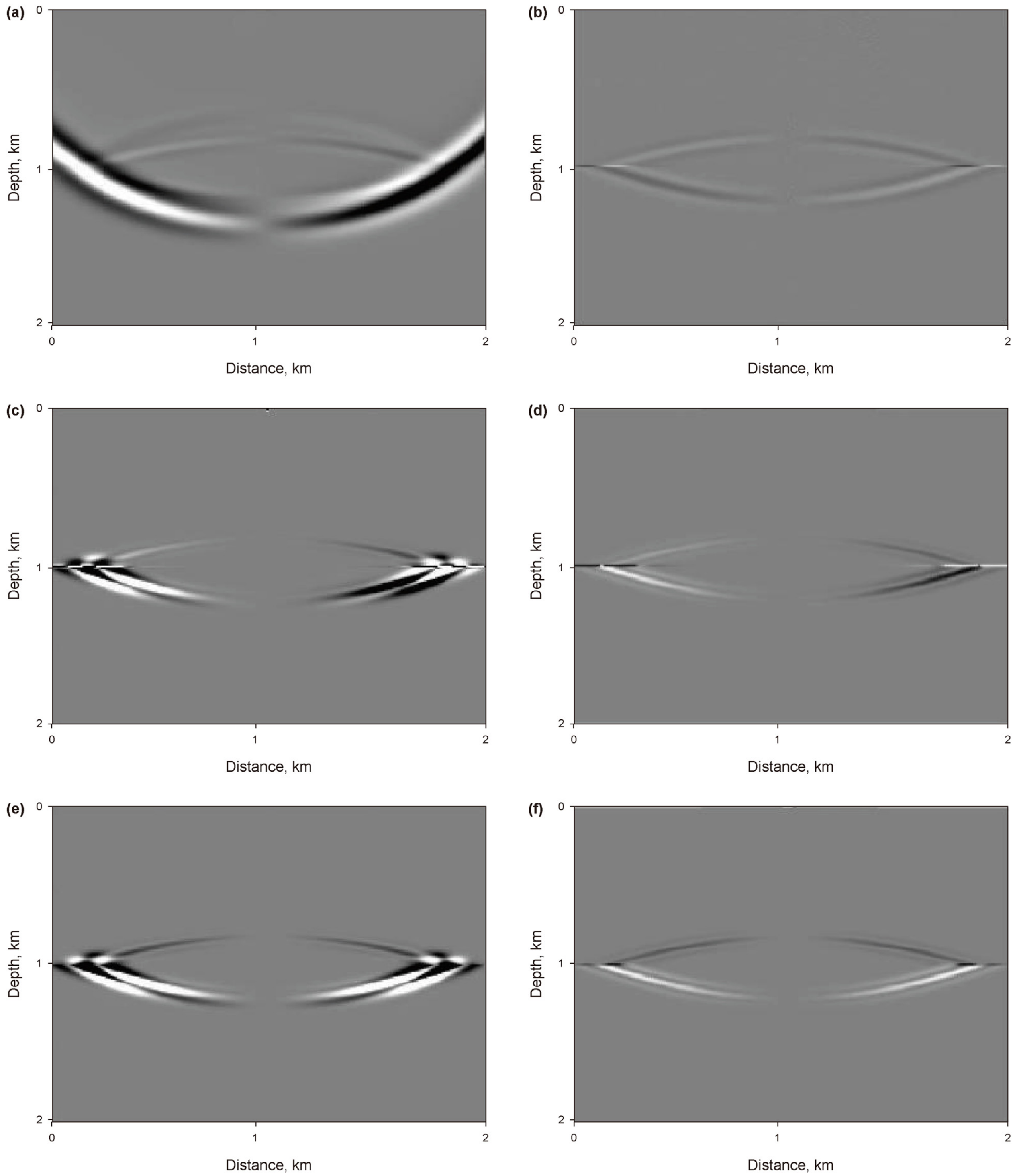

Fig. 3. The snapshots at 0.4 s: The snapshots of stress (τ_{xzs}) **(a)** and S-wave Poynting vector in x component **(c)** and z component **(e)** obtained by conventional method; The snapshots of stress (τ_{xzs}) **(b)** and S-wave Poynting vector in x component **(d)** and z component **(f)** obtained by S-wave equal tensor-based method.

filtering (Wu et al., 2018) to smooth the ADCIGs.

3. Examples

In this section, we will begin by evaluating the accuracy of our developed method in calculating the Poynting vector. Next, we will validate the advantages of our method in extracting ADCIGs from both simple and complex synthetic data, with a focus on enhancing the imaging accuracy of PP waves through angular stacking imaging conditions. Additionally, we will analyze the impact of various parameters on the quality of ADCIGs. It's worth noting that all numerical examples will be implemented using CUDA programming for efficient computation. To minimize storage requirements, we will employ a checkpoint-assisted time reversal reconstruction scheme for the reconstruction of the source wavefield (Symes, 2007). In contrast to the traditional ERTM-based method for

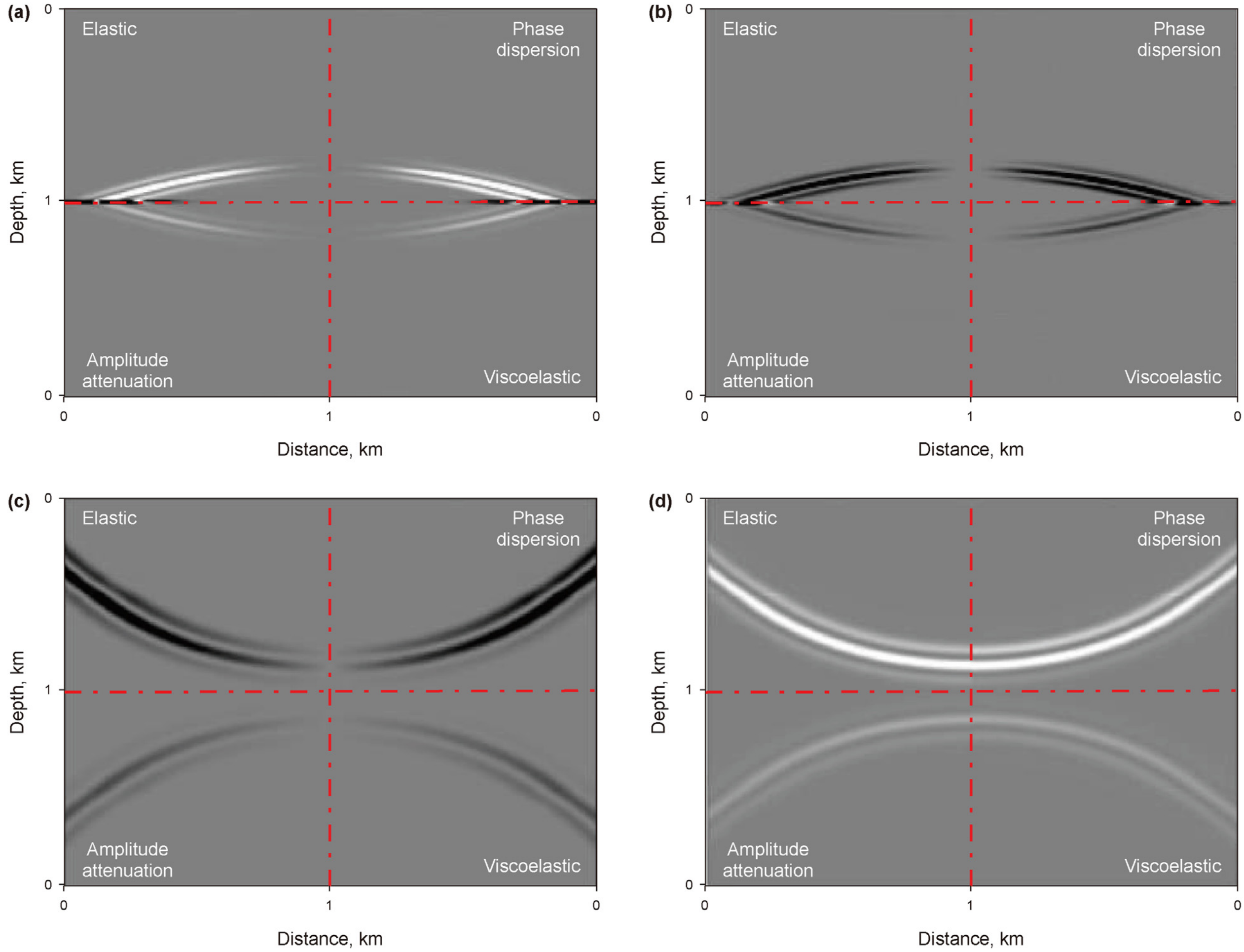

Fig. 4. The snapshots with different attenuation effects at 0.4 s: The S-wave Poynting vector in x component **(a)** and z component **(b)**; The P-wave Poynting vector in x component **(c)** and z component **(d)**.

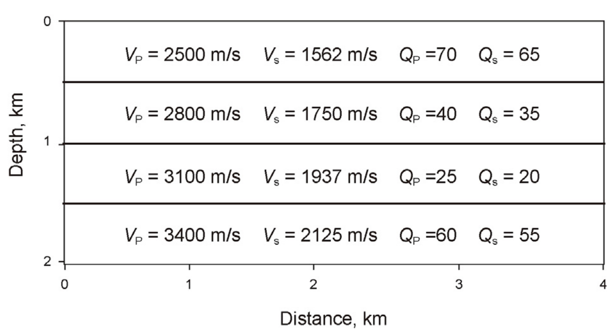

Fig. 5. Viscoelastic parameters of the layer model.

extracting ADCIGs, our developed Q-ERTM method theoretically considers the attenuation effects of seismic waves, which has the potential to improve the accuracy of ADCIGs. In this section, we first evaluate the accuracy of our method in calculating the Poynting vector. Next, we demonstrate the advantages of our method for ADCIG extraction from both simple and complex synthetic data, focusing on enhancing PP wave imaging accuracy through angular stacking imaging conditions. Additionally, we examine the impact of key parameters on ADCIG quality. Notably, all numerical examples are implemented using CUDA programming for efficient computation. To minimize storage requirements, we employ a checkpoint-assisted time reversal reconstruction scheme for the source wavefield reconstruction (Symes, 2007). Unlike the traditional ERTM-based method, our Q-ERTM approach theoretically accounts for seismic wave attenuation, which may improve ADCIG accuracy.

3.1. Calculation of Poynting Vector

In the forward modeling process, we use the velocity and quality factor model depicted in Fig. 2, which includes the specific parameters (V_p, V_p, Q_p, Q_s). The size of parameter model is 2 km × 2 km, with a grid interval of 10 m. A Ricker wavelet with a frequency of 15 Hz serves as the source. The time sampling interval is set to 0.4 ms, and the maximum recording time is 0.8 s. A source is set on the surface at 1 km.

We conduct calculations for the Poynting vector and generate a snapshot of the wavefield and Poynting vector at 0.4 s, which is illustrated in Fig. 3. Initially, we validated the superiority of the S-wave equal tensor-based method. In Fig. 3(a) and (b), we showcase stress (τ_{xzs}) snapshots acquired through traditional methods and those derived from S-wave equal tensor-based method. Fig. 3(a) vividly shows there is P-wave interference in the coupled S-wave wavefield snapshot, resulting in an inaccurate calculation of the S-wave's Poynting vector. Utilizing the S-wave equal tensor-based method, as demonstrated in Fig. 3(b), we successfully isolate the S-wave wavefield, thereby eliminating P-wave interference and

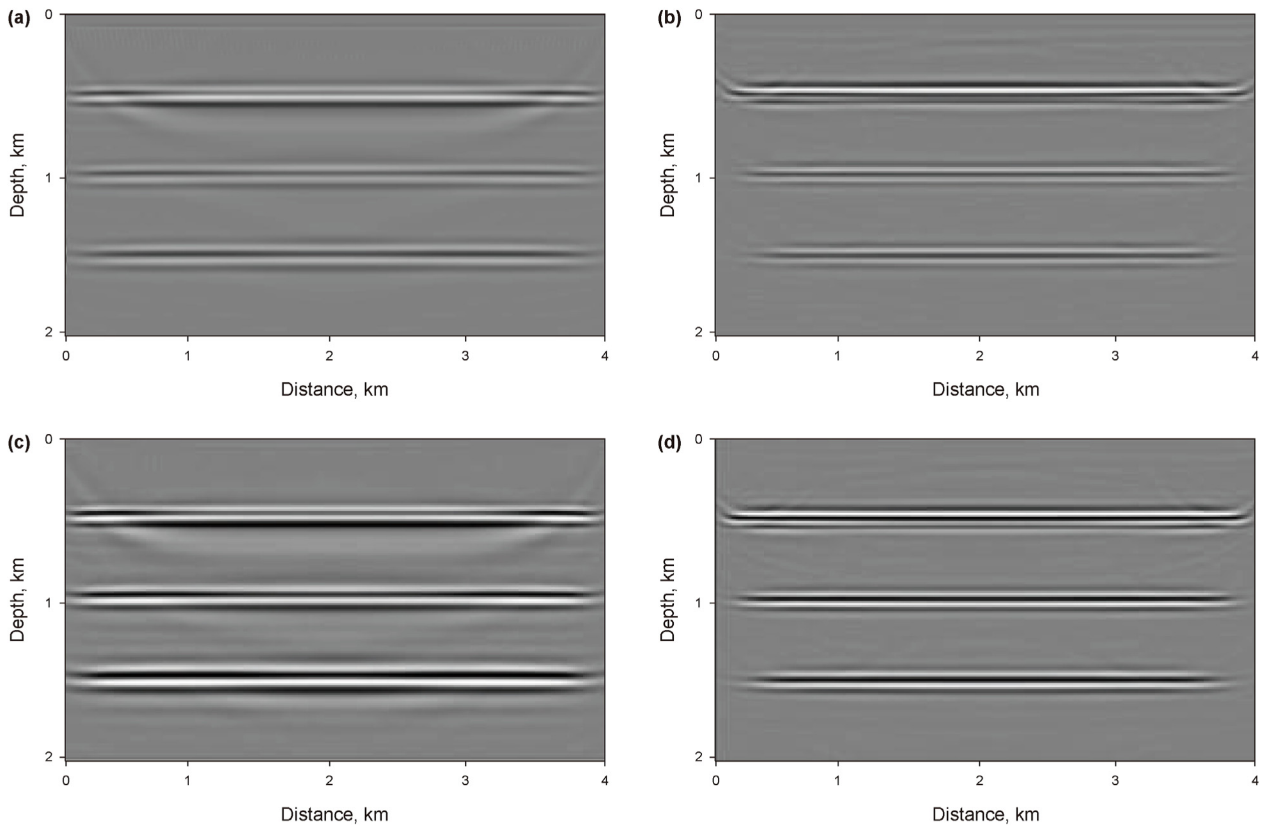

Fig. 6. The migration image of layer model: **(a)** PP image and **(b)** PS image obtained by ERTM; **(c)** PP image and **(d)** PS image obtained by QERTM.

enhancing the accuracy of Poynting vector calculations. Fig. 3(b) displays interface artifacts, reducible through velocity model smoothing or removable via median filtering. Given the migration velocity model's smoothness, these artifacts do not impact the migration process or ADCIGs extraction. Fig. 3(c)–(f) displays the x and z components of the S-wave Poynting vector, obtained by the traditional method and the S-wave equal tensor-based method. Comparing Fig. 3(c), (e) with Fig. 3(d), (f) demonstrates that the S-wave equal tensor-based method, which avoids P-wave interference in stress, yields more accurate Poynting vectors for S-waves in the x and z components. Next, using the parameter models shown in Fig. 2, we evaluate the impact of attenuation effects, such as amplitude attenuation and phase disturbance, on the Poynting vector, as illustrated in Fig. 4. It illustrates how the attenuation effect, which influences both the phase and amplitude of seismic waves, impacts the Poynting vector and thus affects ADCIG extraction. Therefore, studying ADCIG extraction from viscoelastic media is of significant importance.

3.2. The layer model

We initially employ a layered model to evaluate the impact of viscoelastic media on ADCIGs. The primary parameters are illustrated in Fig. 5, which also shows that the second layer is characterized as a strongly attenuating layer. The dimensions of the parameter model are 2 km in length and 4 km in width, with each grid 10 m. A total of 100 sources and 400 receivers are evenly dispersed across the surface to acquire the observed data. The source employs a Ricker wavelet with a frequency of 18 Hz and a time sampling interval of 1 ms.

We initially conduct tests to assess the impact of viscoelastic media on migration imaging, with the results from both ERTM and QERTM illustrated in Fig. 6. In Fig. 6(a) and (b), the PP-image and PS-images from ERTM show weaker reflective events due to the lack of compensation capability in this method. Conversely, Fig. 6(c) and (d) show that the QERTM-based method effectively compensates for the Q effect in seismic wave propagation, enhancing the energy of reflective events, particularly in deep imaging.

Subsequently, we assess the performance of ADCIGs ($0^\circ - 60^\circ$) extraction methods in a comparative analysis of ERTM and QERTM, as presented in Fig. 7. Fig. 7(a) and (b) respectively showcase a comparison of PP-ADCIGs and PS-ADCIGs at CDP = 200. Initially, due to the attenuation compensation effect, the QERTM method effectively enhances the deep energy in ADCIGs which is similar with migration image. Concurrently, the attenuation compensation effect results in more concentrated energy in large angle gathers from ADCIGs, particularly in deeper layers of PS-ADCIGs. Moreover, owing to the limited coverage of seismic data, the observations mentioned are more evident in the ADCIG at CDP = 350, as shown in Fig. 7(c) and (d). The test has validated that using the Poynting vector method for extracting ADCIGs is notably effective in viscoelastic media, particularly achieving superior results in deeper parts and at larger angles.

3.3. The hess model

To further evaluate practicality in more complex model with our method, we employ the Hess model for testing. Fig. 8 presents essential model parameters, including the P and S velocity models, as well as the quality factor models Qp and Qs. Notably, it showcases the presence of two distinct and prominent attenuation layers. Specifically, the dimensions of these models are 2.18 km and 3.62 km with a grid spacing of 10 m. The observational system consists of 120 sources and 362 receivers, uniformly distributed

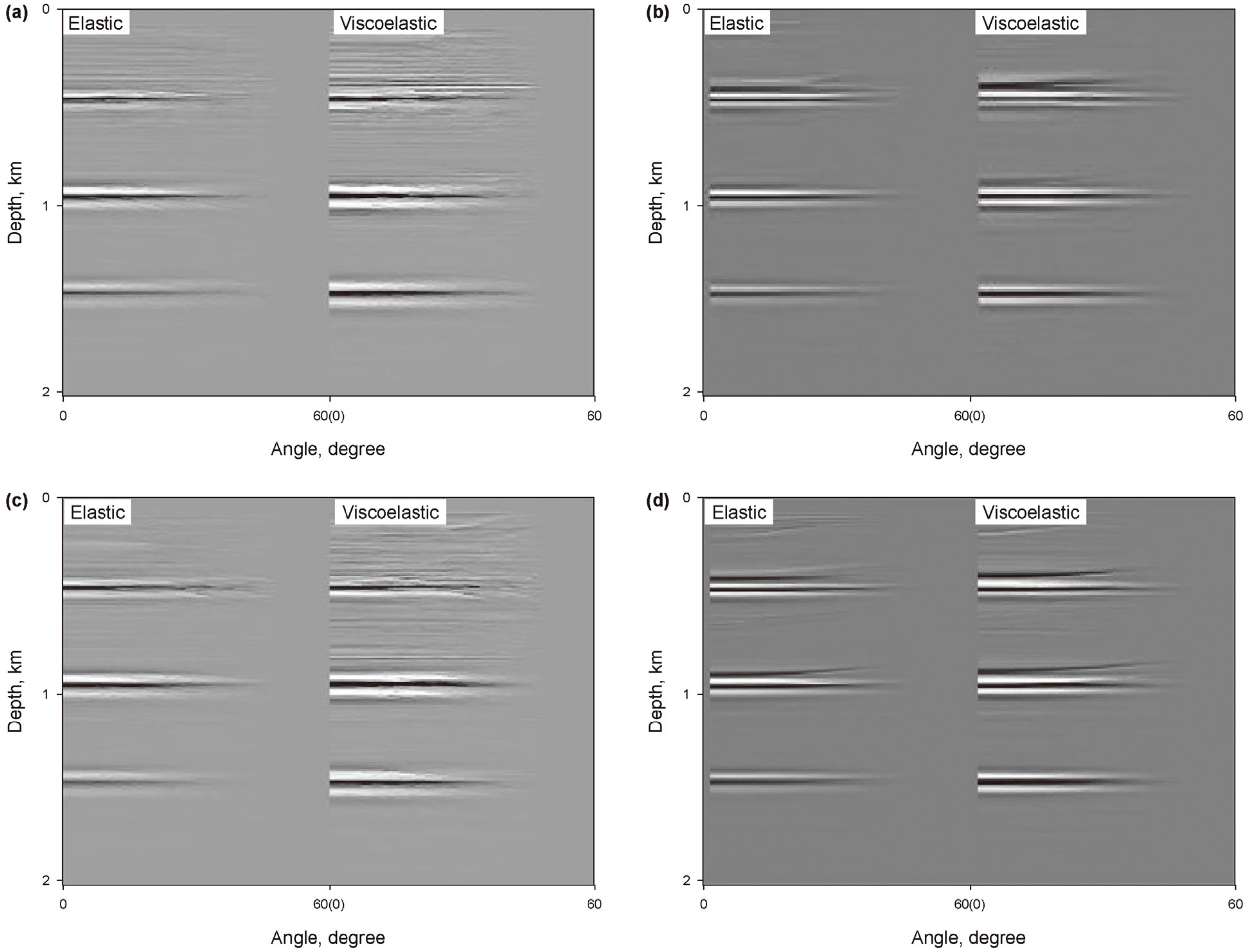

Fig. 7. The ADCIGs of layer model: **(a)** PP-ADCIGs and **(b)** PS-ADCIGs at CDP = 200; **(c)** PP-ADCIGs and **(d)** PS-ADCIGs at CDP = 350.

across the surface to record observational data. The source is a Ricker wavelet with a central frequency of 20 Hz. The temporal sampling interval is configured at 0.4 ms, with a maximum recording time of 1.6 s.

Fig. 9 presents the elastic wave migration images obtained by ERTM with non-compensated viscoelastic data and migration images obtained by QERTM. It becomes evident that the images beneath the attenuation layer in Fig. 9(a) and (b) display a noticeable degree of blurriness and a corresponding decrease in energy. In contrast, Fig. 9(c) and (d) demonstrate a substantial improvement in this regard, which can significantly enhance the imaging accuracy beneath the attenuation layer. Furthermore, the migration images of salt model boundaries acquired by QERTM display enhanced resolution, with a particularly notable improvement in PS-image. The vertical profile at CDP = 190 further clearly demonstrates the compensation effect of QERTM on PP image (Fig. 10(a)) and PS image (Fig. 10(b)). Subsequently, we conduct an analysis of the influence of the proposed method on the extraction of ADCIGs. In Fig. 11, we showcase the ADCIGs at CDP = 260, which are obtained by QERTM and ERTM, respectively. Both PP-ADCIGs (Fig. 11(a)) and PS-ADCIGs (Fig. 11(b)) correspond well with the reflection layer (red line). However, compared to ADCIGs obtained from ERTM, QERTM achieves more effective compensation for deep energy and offers more comprehensive information at larger angles.

3.4. The BP gas model

To further demonstrate the adaptability of this method to complex models, we further apply this method to the classic BP gas model. The velocity models for P- and S-waves, along with their respective Quality factors Q, are illustrated in Fig. 12. These models use a grid of 200 × 500 with a spacing of 10 m. A Ricker wavelet with frequency 20 Hz, is utilized as the source wavelet. The sampling time is set to 3 s, with a time interval of 0.6 ms.

We conduct QERTM and ERTM imaging on this synthetic data separately, and the obtained images are displayed in Fig. 13. From Fig. 13, it is clearly observable that, owing to the incorporation of attenuation compensation, the deep energy in QERTM imaging is significantly enhanced in comparison to ERTM imaging. This enhancement is especially notable in the areas below the attenuation chimney (highlighted by yellow boxes) and around acute structures (indicated with red arrows). Additionally, as we compare PP-ADCIGs and PS-ADCIGs at CDP = 150 in Fig. 14, it becomes apparent that the event axis of ADCIG closely aligns with the reflection layer (red line). Furthermore, because of the attenuation compensation effect, QERTM outperforms ERTM by better compensating for attenuation in the ADCIGs and enhancing energy at large angles.

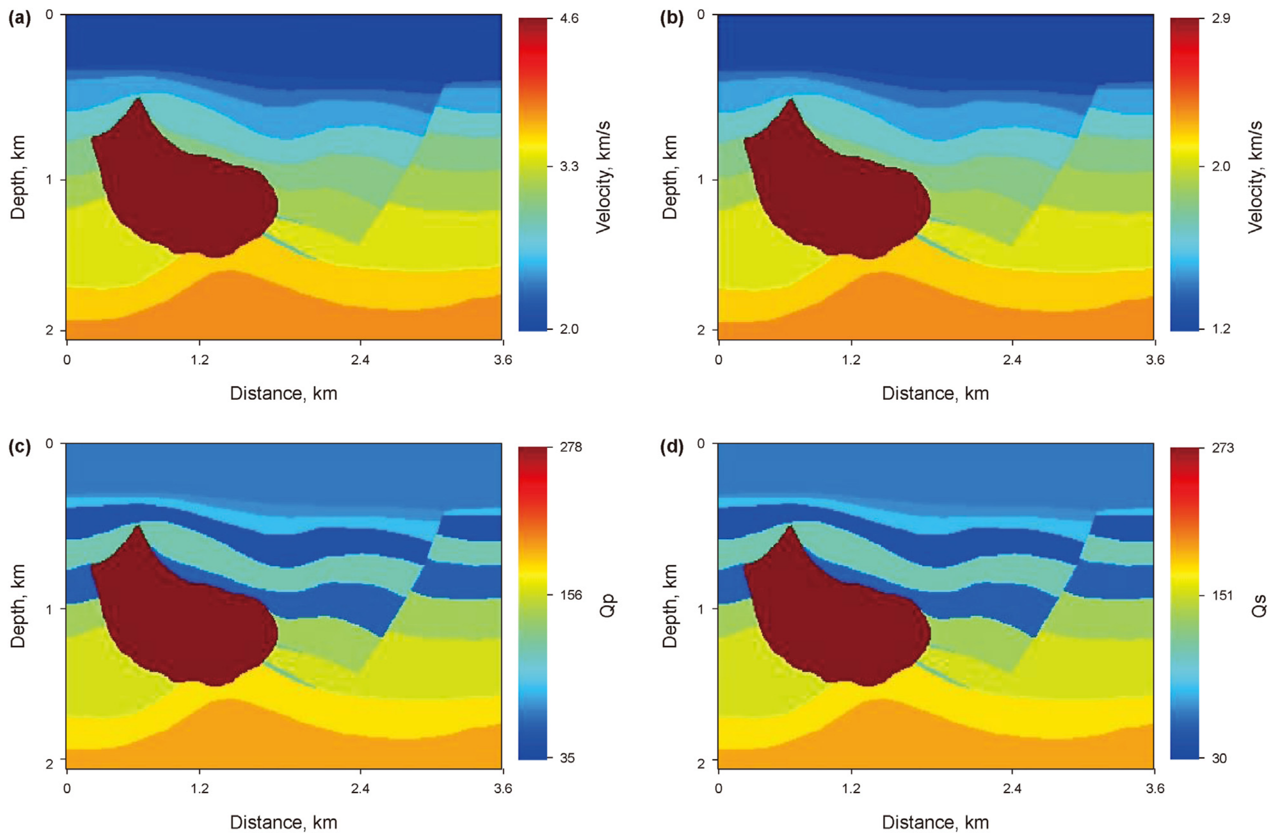

Fig. 8. Viscoelastic parameters of the Hess model: **(a)** P-wave velocity and **(b)** S-wave velocity; Quality factor Q of P-wave **(c)** and S-wave **(d)**.

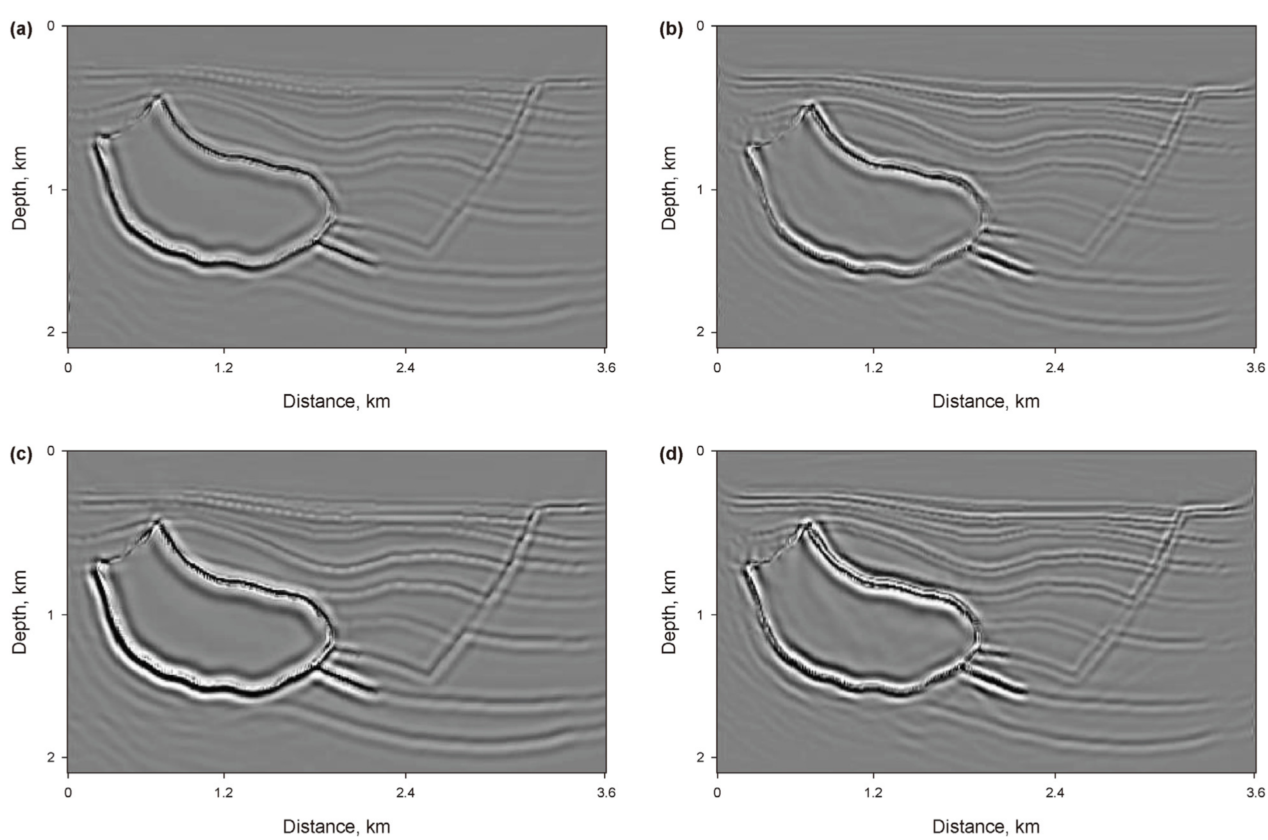

Fig. 9. The migration image of Hess model: **(a)** PP image and **(b)** PS image obtained by ERTM; **(c)** PP image and **(d)** PS image obtained by QERTM.

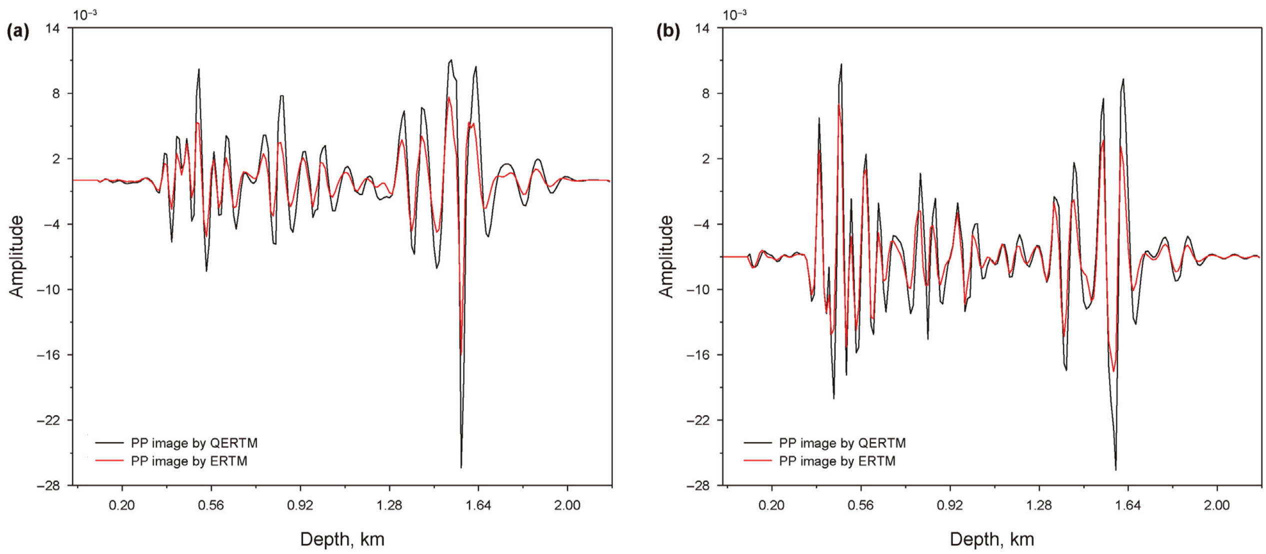

Fig. 10. The vertical profile at CDP = 190 of PP image **(a)** and PS image **(b)**.

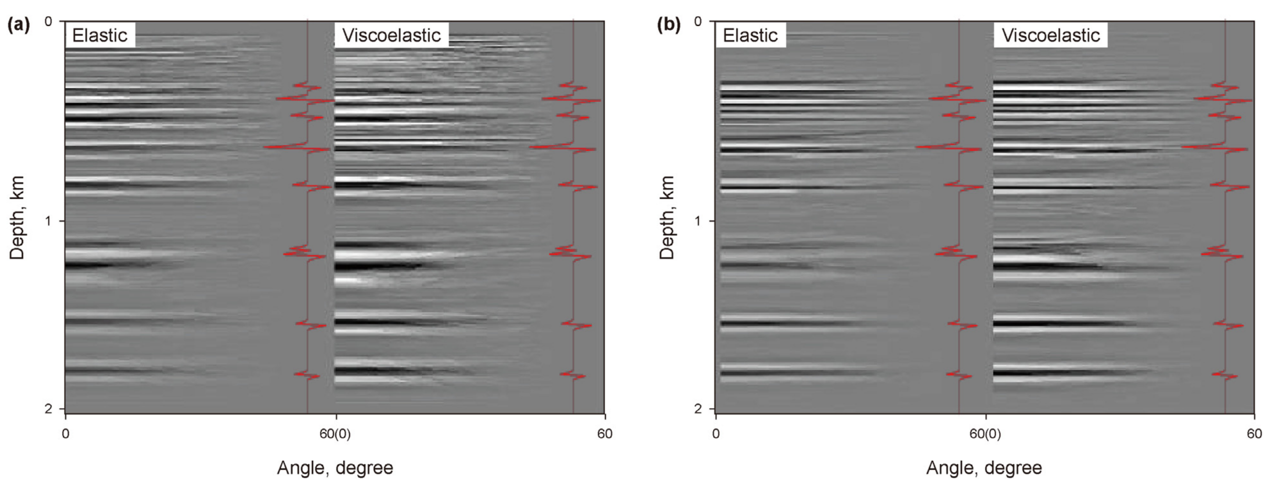

Fig. 11. The ADCIGs of Hess model at CDP = 260: **(a)** PP-ADCIGs and **(b)** PS-ADCIGs.

3.5. *The influence of parameters on ADCIGs*

In viscoelastic media, the quality factor significantly influences the propagation of seismic waves. Consequently, this paper uses the layer model of section 3.2 to examines the impact of the quality factor on ADCIGs. The quality factor Q parameters, which are used to migration, are configured as follows in Table 1. Specifically, we set up two cases: the quality factor Q values are all less than the true values (small case), and the quality factor Q values are all greater than the true values (big case). We use the true values as the standard values. Because deep Q-value inversion has always been a challenge in tomography and full waveform inversion, we create a greater difference in the values of the last layer to further simulate this challenge. Fig. 15 displays the ADCIGs from CDP = 250. By comparison, it can be found that although a smaller particle quality factor QQQ used for migration is beneficial for energy compensation in deep PP-ADCIG and PS-ADCIG, it may cause wavefield instability, negatively impacting their resolution. Concurrently, it also impacts the focusing of large angle (green arrow) ADCIGs. Furthermore, when the quality factor Q is excessively high, it fails to achieve satisfactory compensation, yielding migration similar to the uncompensated ADCIGs obtained by ERTM. This observation demonstrates that within the inversion process, opting for a relatively high Q model as the initial value for inversion parameters is optimal, as it aids in enhancing the accuracy of viscoelastic parameter inversion.

4. Discussion

Currently, there are three categories for extracting angle-domain common-image gathers (ADCIGs) during reverse-time migration (Vyas et al., 2011a): direction-vector-based methods (DVB), local-plane-wave decomposition methods (LPWD), and local-shift imaging condition methods (LSIC). The LPWD and LSIC, utilizing some transforms method, yielding highly comparable angle gathers (Jin et al., 2015). The quality of ADCIGs generated by these techniques is contingent upon the size of the local window in which the transformations are executed. In smaller windows, both approaches produce ADCIGs with minimal noise yet reduced angular resolution; conversely, larger windows facilitate higher angular resolution at the expense of introducing smeared artifacts (Xu et al., 2011). As a comparison, the ADCIGs based on DVB have

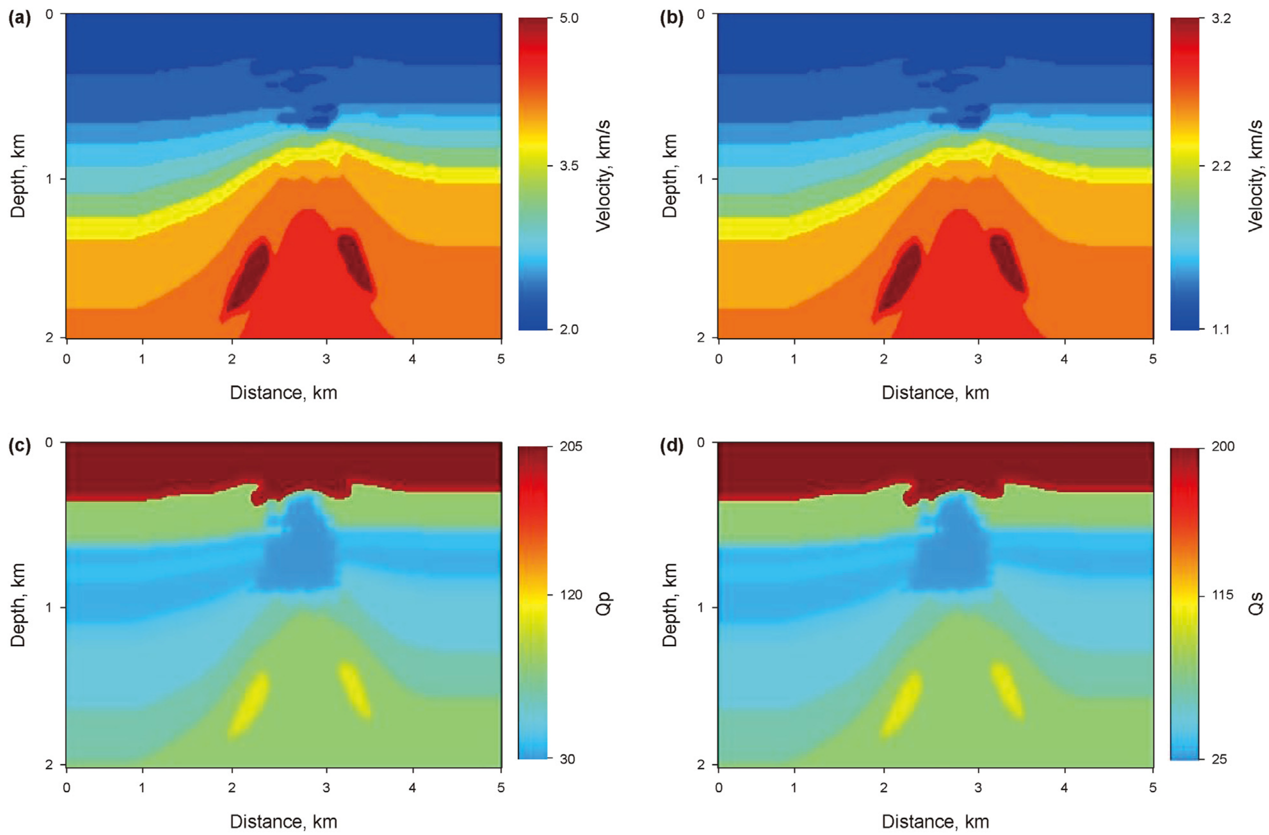

Fig. 12. Viscoelastic parameters of the BP gas model: **(a)** P-wave velocity and **(b)** S-wave velocity; Quality factor Q of P-wave **(c)** and S-wave **(d)**.

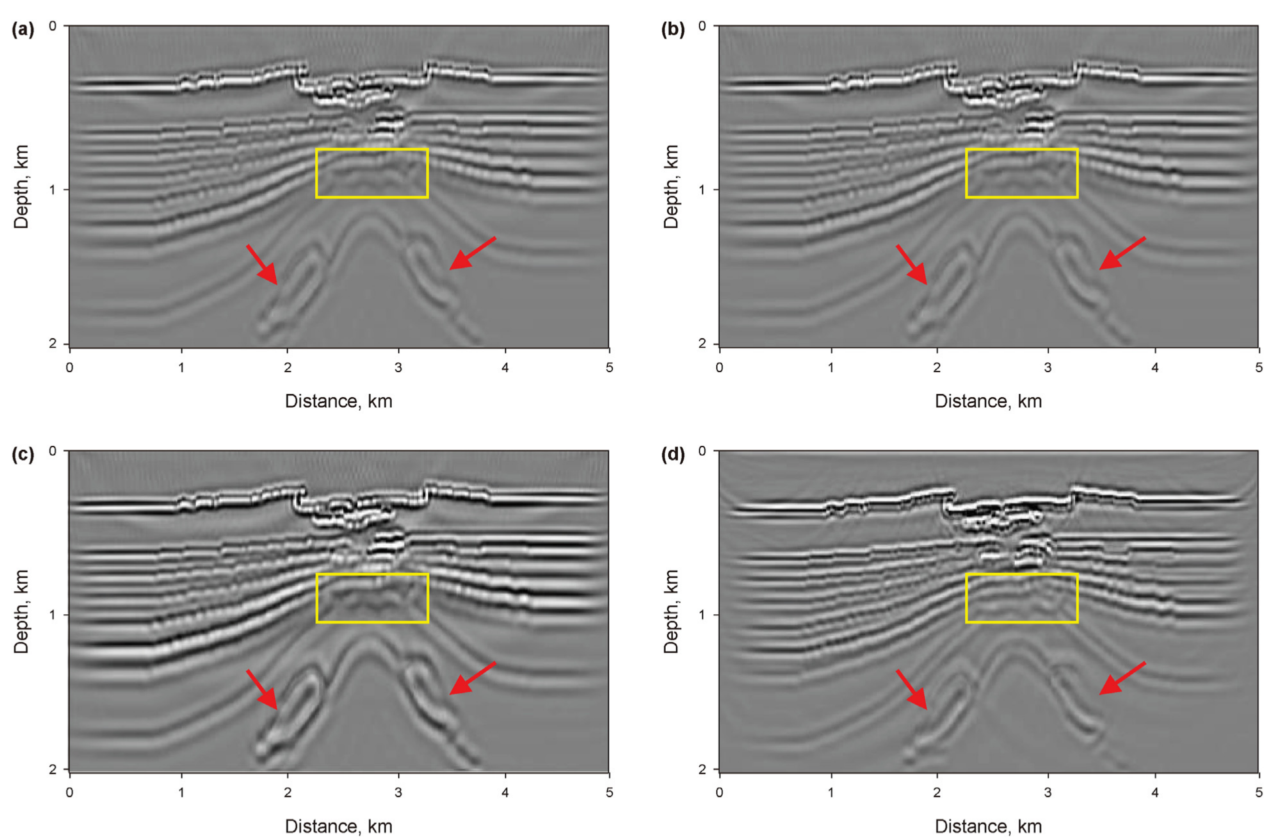

Fig. 13. The migration image of the BP gas model: **(a)** PP image and **(b)** PS image obtained by ERTM; **(c)** PP image and **(d)** PS image obtained by QERTM.

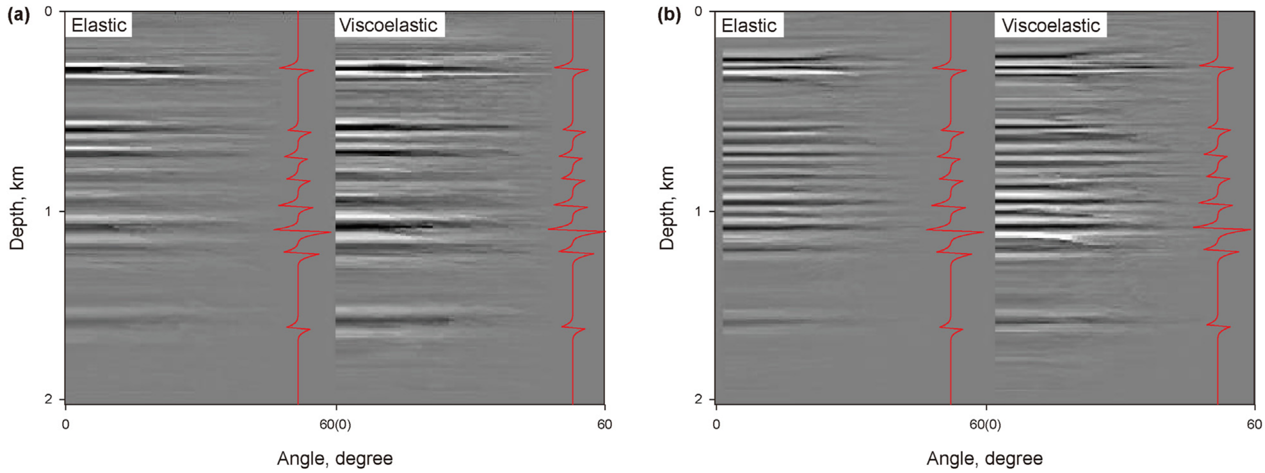

Fig. 14. The ADCIGs of the BP gas model: at CDP = 150: **(a)** PP-ADCIGs and **(b)** PS-ADCIGs.

Table 1
The quality factor Q parameters used for migration.

Case	Qp (from top to bottom in four layers)	Qs (from top to bottom in four layers)
Small	40, 15, 40, 15	35, 10, 35, 10
Large	100, 75, 110, 100	95, 70, 105, 95

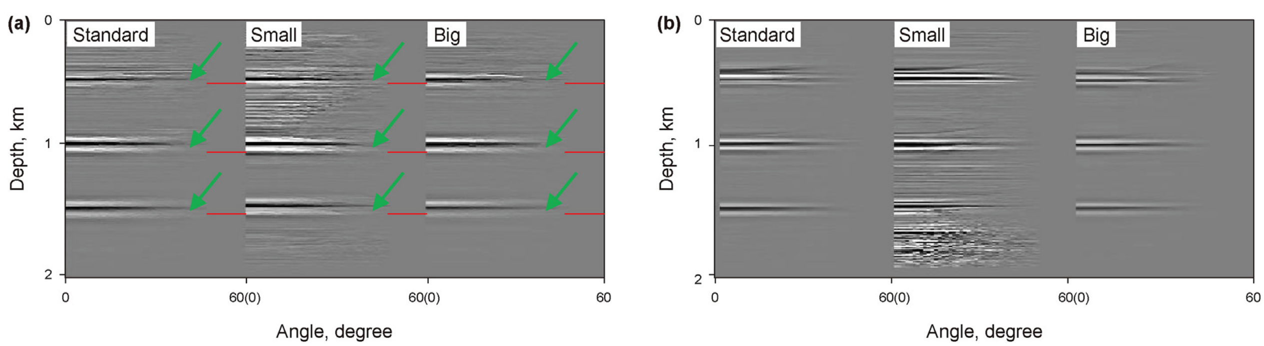

Fig. 15. PP-ADCIGs **(a)** and PS-ADCIGs **(b)** at CDP = 250 with different quality factor Q.

the highest angle resolution. In addition, the propagation angles of the source and receiver can be calculated using the Poynting vector-based method (Yoon and Marfurt, 2006), the polarization vector-based method (Zhang and McMechan, 2011a), and the instantaneous wavenumber vector based method (Zhang and McMechan, 2011b). Since both the Poynting vector-based method and the polarization vector-based method rely on amplitude gradients and yield identical (or opposite) directions, they are regarded as variations of the same methodology, namely the amplitude-gradient approach. The method utilizing the instantaneous wavenumber vector relies on the instantaneous phase of the wave field in the spatial domain, as opposed to the amplitude. At present, there exists no quantitative calculation available for comparison among these methods. In terms of improving resolution using DVB-based method, two primary methods exist for enhancing the resolution of ADCIGs (Luo et al., 2010). One approach involves calculating the propagation angles of both the source and the receiver, which includes averaging the Poynting vectors in space over four time periods of the source wavelet (Yoon et al., 2011), a least squares solution over a time window (Yan and Ross, 2013), or smoothing the Poynting vectors in the space domain (Dickens and Winbow, 2011). These techniques can significantly enhance both the resolution and the signal-to-noise ratio of ADCIGs. An alternative method presently utilized is the filtering-based approach, which encompasses mean filtering, Gaussian smoothing, and Laplace filtering (Chang and McMechan, 1986; Dafni and Symes, 2016). These methods have the advantages of high computational efficiency and significant resolution improvement. Due to the fact that this paper primarily analyzes the influence of attenuative media and adopts the correct migration velocity, we have chosen the second method (triangular smoothing filtering) to improve resolution, balancing efficiency and accuracy.

In addition, research on ADCIGs is primarily concentrated on ensuring stability in the calculation of the Poynting vector (Vyas et al., 2011b). This focus is due to the nature of the Poynting vector, which is derived from the product of the time and spatial derivatives of the wave field. At the local extremum of the seismic wave field, these two derivatives equate to zero, rendering the Poynting vector incapable of providing the propagation direction at such points. The triangular smoothing filter selected is also capable of effectively addressing this issue (Yoon, 2017; Wu et al., 2018). In addition, commonly used methods include optical flow (OF) strategies (Zhang, 2014), and time shifting approaches (Tang et al., 2017). Enhancing the stability of Poynting vector calculations in viscoelastic media is also a key focus of our future research (Li et al., 2023).

5. Conclusions

We develop a Poynting vector-based method for extracting ADCIGs in viscoelastic media. Specifically, by introducing the viscoelastic effect of the medium during ADCIGs extraction, we can achieve more accurate Poynting vectors compared to traditional methods. This results in more precise calculation of P-wave and S-wave angles. In addition, for the S-wave's Poynting vector calculation, we utilize the S-wave equal tensor to improve the accuracy of S-wave stress, leading to a more precise S-wave Poynting vector. Numerical experiments reveal that, in comparison to traditional methods without compensation, the introduction of Q-compensation effectively compensates for the deep energy in offset imaging and ADCIG, and enhances the large-angle accuracy of ADCIG. Finally, our examination focuses on the impact of quality factors on the extraction of ADCIGs. Finally, we assess the impact of quality factors on the ADCIGs extraction process. We observe that smaller quality factors tend to cause overcompensation, thereby influencing the accuracy of ADCIGs more significantly than larger inversion quality factors Q.

Data availability

Data will be made available on request.

CRediT authorship contribution statement

Wen-Bin Tian: Writing – original draft, Validation, Methodology. **Yang Liu:** Writing – review & editing, Supervision, Funding acquisition. **Jiang-Tao Ma:** Investigation, Data curation.

Declaration of competing interest

The authors declare that they have no known competing financial interests or personal relationships that could have appeared to influence the work reported in this paper.

Acknowledgements

This work is supported by the National Natural Science Foundation of China (NSFC) under contract number 42274147 and 41874144.

Appendix A

The reverse time migration imaging in viscoelastic media includes amplitude compensation and phase correction. However, amplitude compensation during the migration process frequently makes the divergence of high-frequency noise, leading to numerical instability. In this paper, we employ adaptive stabilization techniques to address this issue (Wang et al., 2018b, 2019). The adaptive stabilization operator can be represented as:

$$S(\mathbf{k},t)=\frac{1}{1+\sigma^2 e^{2\xi_2(\mathbf{k})t}}, \tag{A-1}$$

where σ represents a constant value in this equation, $\xi_2(\mathrm{k})t$ can be described as:

$$\xi_2(\mathrm{k})t=\frac{1}{2}c_0^{2\gamma-1}\omega_0^{-2\gamma}\sin(\pi\gamma)c^2|\mathbf{k}|^{2\gamma+1}. \tag{A-2}$$

This coefficient will be employed to facilitate absorption attenuation within the all reverse time extension process, which can be described as:

$$S(k,l\Delta t)=\begin{cases}\dfrac{1}{1+\sigma^2 e^{2\xi_2(\mathbf{k})\Delta t}}, & l=1,\\[2ex] \dfrac{1+\sigma^2 e^{2\xi_2(\mathbf{k})(l-1)\Delta t}}{1+\sigma^2 e^{2\xi_2(\mathbf{k})l\Delta t}}, & l=2,3,\ldots,n,\end{cases} \tag{A-3}$$

where l is the lth time steps. In the viscoelastic equation, both P-wave and S-wave components share identical expression forms, allowing for the direct application of the adaptive stabilization operator to their backpropagated wave fields. This approach effectively addresses the instability issues associated with amplitude compensation in QERTM.

References

Alkhalifah, T., Fomel, S., 2009. Angle gathers in wave-equation imaging for VTI media. In: 79th Annual International Meeting, SEG, Expanded Abstracts, pp. 4027–4031. https://doi.org/10.1190/1.3255453.

Biondi, B., 2007. Angle-domain common-image gathers from anisotropic migration. Geophysics 72 (2), S81–S91. https://doi.org/10.1190/1.2430561.

Biondi, B., Symes, W.W., 2004. Angle-domain common-image gathers for migration velocity analysis by wavefield-continuation imaging. Geophysics 69 (5), 1283–1298. https://doi.org/10.1190/1.1801945.

Biondi, B., Tisserant, T., 2004. 3D angle-domain common-image gathers for migration velocityanalysis. Geophys. Prospect. 52 (6), 575–591. https://doi.org/10.1111/j.1365-2478.2004.00444.x.

Canning, A., Malkin, A., 2009. Azimuthal AVA analysis using full-azimuth 3D angle gathers. In: 79th Annual International Meeting, SEG, Expanded Abstracts, pp. 256–259. https://doi.org/10.1190/1.3255379.

Carcione, J.M., Cavallini, F., Mainardi, F., et al., 2002. Time-domain modeling of constant-Q seismic waves using fractional derivatives. Pure. Appl. Geophys. 159, 1719–1736. https://doi.org/10.1007/s00024-002-8705-z.

Chang, W.F., McMechan, G.A., 1986. Reverse-time migration of offset vertical seismic profiling data using the excitation-time imaging condition. Geophysics 51, 67–84. https://doi.org/10.1190/1.1442041.

Chang, W.F., McMechan, G.A., 1987. Elastic reverse-time migration. Geophysics 52 (10), 1365–1375. https://doi.org/10.1190/1.1442249.

Chen, H., Zhang, L., Zhou, H., 2023. Fractional laplacians viscoelastic wave equation low-rank temporal extrapolation. Front. Earth Sci. 10, 1044823. https://doi.org/10.3389/feart.2022.1044823.

Chen, H., Zhou, H., Li, Q., et al., 2016. Two efficient modeling schemes for fractional Laplacian viscoacoustic wave equation. Geophysics 81 (5), T233–T249. https://doi.org/10.1190/geo2015-0660.1.

Chen, P., Villa, U., Ghattas, O., 2019. Taylor approximation and variance reduction for PDE-constrained optimal control under uncertainty. J. Comput. Phys. 385, 163–186. https://doi.org/10.1016/j.jcp.2019.01.047.

Chen, W., Holm, S., 2004. Fractional Laplacian time-space models for linear and nonlinear lossy media exhibiting arbitrary frequency power-law dependency. J. Acoust. Soc. Am. 115 (4), 1424–1430. https://doi.org/10.1121/1.1646399.

Dafni, R., Symes, W.W., 2016. Kinematic artifacts in the subsurface-offset extended image and their elimination by a dip-domain specularity filter. Geophysics 81 (6), S477–S495. https://doi.org/10.1190/geo2016-0115.1.

Deng, F., McMechan, G.A., 2008. Viscoelastic true-amplitude prestack reverse-time depth migration. Geophysics 73 (4), S143–S155. https://doi.org/10.1190/1.2938083.

Dickens, T.A., winbow, G., 2011. RTM angle gathers using Poynting vectors. In: 81th Annual International Meeting, SEG, Expanded Abstracts, pp. 3109–3113. https://doi.org/10.1190/1.3627841.

Du, Q., Guo, C., Zhao, Q., et al., 2017. Vector-based elastic reverse time migration based on scalar imaging condition. Geophysics 82 (2), S111–S127. https://doi.org/10.1190/geo2016-0146.1.

Du, Q., Zhu, Y., Ba, J., 2012. Polarity reversal correction for elastic reverse time migration. Geophysics 77 (2), S31–S41. https://doi.org/10.1190/geo2011-0348.1.

Gong, T., Nguyen, B.D., McMechan, G.A., 2016. Polarized wavefield magnitudes with optical flow for elastic angle-domain common-image gathers. Geophysics 81 (4), S239–S251. https://doi.org/10.1190/geo2011-0348.1.

Guo, P., McMechan, G.A., Guan, H., 2016. Comparison of two viscoacoustic propagators for Q-compensated reverse time migration. Geophysics 81 (5), S281–S297. https://doi.org/10.1190/geo2015-0557.1.

Hao, Q., Greenhalgh, S., 2019. The generalized standard-linear-solid model and the corresponding viscoacoustic wave equations revisited. Geophys. J. Int. 219 (3),

1939–1947. https://doi.org/10.1093/gji/ggz407.
Hu, J., Wang, H., Wang, X., 2016. Angle gathers from reverse time migration using analytic wavefield propagation and decomposition in the time domain. Geophysics 81 (1), S1–S9. https://doi.org/10.1190/geo2015-0050.1.
Hu, T., Liu, H., Guo, X., et al., 2019. Analysis of direction-decomposed and vector-based elastic reverse time migration using the Hilbert transform. Geophysics 84 (6), S599–S617. https://doi.org/10.1190/geo2018-0324.1.
Jin, H., McMechan, G.A., Guan, H., 2014. Comparison of methods for extracting ADCIGs from RTM. Geophysics 79 (3), S89–S103. https://doi.org/10.1190/geo2013-0336.1.
Jin, H., McMechan, G.A., Nguyen, B., 2015. Improving input/output performance in 2D and 3D angle-domain common-image gathers from reverse time migration. Geophysics 80 (2), S65–S77. https://doi.org/10.1190/geo2014-0209.1.
Koren, Z., Ravve, I., Gonzalez, G., et al., 2008. Anisotropic local tomography. Geophysics 73 (5), VE75–VE92. https://doi.org/10.1190/1.2953979.
Li, F., Gao, J., Gao, Z., et al., 2021. Angle domain common image gathers from reverse time migration by combining the Poynting vector with directional decomposition. Geophys. Prospect. 69 (4), 799–820. https://doi.org/10.1111/1365-2478.13064.
Li, Q., Zhou, H., Zhang, Q., et al., 2016a. Efficient reverse time migration based on fractional Laplacian viscoacoustic wave equation. Geophys. J. Int. 204 (1), 488–504. https://doi.org/10.1093/gji/ggv456.
Li, Z., Ma, X., Fu, C., et al., 2016b. Wavefield separation and polarity reversal correction in elastic reverse time migration. J. Appl. Geophys. 127, 56–67. https://doi.org/10.1016/j.jappgeo.2016.02.012.
Li, Z., Wang, J., Ma, X., et al., 2023. Calculation of the stable Poynting vector using the first-order temporal derivative of the seismic wavefield. Geophysics 88 (1), S17–S25. https://doi.org/10.1190/geo2021-0736.1.
Liu, Q., 2019. Dip-angle image gather computation using the Poynting vector in elastic reverse time migration and their application for noise suppression. Geophysics 84 (3), S159–S169. https://doi.org/10.1190/geo2018-0229.1.
Liu, R., Qin, N., Yin, X., 2017. ADCIGs extraction and reflection tomography modeling for elastic wave. J. Appl. Geophys. 143, 203–211. https://doi.org/10.1016/j.jappgeo.2017.04.006.
Liu, S.Y., Wang, H.Z., Liu, T.C., et al., 2015. Kirchhoff PSDM angle-gather generation based on the traveltime gradient. Appl. Geophys. 12 (1), 64–72. https://doi.org/10.1007/s11770-014-0470-8.
Luo, M., Lu, R., Winbow, G., et al., 2010. A comparison of methods for obtaining local image gathers in depth migration. In: 80th Annual International Meeting, SEG, Expanded Abstracts, pp. 3247–3251. https://doi.org/10.1190/1.3513522.
McGarry, R., Qin, Y., 2013. Direction-vector-based angle gathers from anisotropic elastic RTM. In: 83th Annual International Meeting, SEG, Expanded Abstracts, pp. 3820–3824. https://doi.org/10.1190/segam2013-0949.1.
Moradi, S., Innanen, K.A., 2017. Born scattering and inversion sensitivities in viscoelastic transversely isotropic media. Geophys. J. Int. 211 (2), 1177–1188. https://doi.org/10.1093/gji/ggx363.
Mosher, C.C., Foster, D.J., Hassanzadeh, S., 1997. Common angle imaging with offset plane waves. In: 67th Annual International Meeting, SEG, Expanded Abstracts, pp. 1379–1382. https://doi.org/10.1190/1.1885663.
Robertsson, J.O., Blanch, J.O., Symes, W.W., 1994. Viscoelastic finite-difference modeling. Geophysics 59 (9), 1444–1456. https://doi.org/10.1190/1.1443701.
Sava, P.C., Fomel, S., 2003. Angle-domain common-image gathers by wavefield continuation methods. Geophysics 68 (3), 1065–1074. https://doi.org/10.1190/1.1581078.
Sava, P., Biondi, B., 2004. Wave-equation migration velocity analysis. I. Theory. Geophys. Prospect. 52 (6), 593–606. https://doi.org/10.1111/j.1365-2478.2004.00447.x.
Song, G., Zhang, X., Wang, Z., et al., 2020. The asymptotic local finite-difference method of the fractional wave equation and its viscous seismic wavefield simulation. Geophysics 85 (3), T179–T189. https://doi.org/10.1190/geo2019-0066.1.
Soubaras, R., 2003. Angle gathers for shot-record migration by local harmonic decomposition. In: 73th Annual International Meeting, SEG, Expanded Abstracts, pp. 889–892. https://doi.org/10.1190/1.1818083.
Sun, C., Qiao, Z., Wu, D., et al., 2017. Modeling of wave equation with fractional derivative using optimal finite-difference method in constant-Q attenuation media. Acta Seismol. Sin. 39 (3), 343–355. https://doi.org/10.11939/jass.2017.03.004.
Sun, J., Zhu, T., 2018. Strategies for stable attenuation compensation in reverse-time migration. Geophys. Prospect. 66 (3), 498–511. https://doi.org/10.1111/1365-2478.12579.
Sun, J., Zhu, T., Fomel, S., 2015. Viscoacoustic modeling and imaging using low-rank approximation. Geophysics 80 (5), A103–A108. https://doi.org/10.1190/geo2015-0083.1.
Sun, R., McMechan, G.A., Hsiao, H.H., et al., 2004. Separating P-and S-waves in prestack 3D elastic seismograms using divergence and curl. Geophysics 69 (1), 286–297. https://doi.org/10.1190/1.1649396.
Symes, W.W., 2007. Reverse time migration with optimal checkpointing. Geophysics 72 (5), SM213–SM221. https://doi.org/10.1190/1.2742686.
Tang, C., McMechan, G.A., 2016. Multidirectional slowness vector for computing angle gathers from reverse time migration. Geophysics 81 (2), S55–S68. https://doi.org/10.1190/geo2015-0134.1.
Tang, C., McMechan, G.A., Wang, D., 2017. Two algorithms to stabilize multidirectional Poynting vectors for calculating angle gathers from reverse time migration. Geophysics 82 (2), S129–S141. https://doi.org/10.1190/geo2016-0101.1.
Vyas, M., Du, X., Mobley, E., et al., 2011a. Methods for computing angle gathers using RTM. In: 73rd Annual International Conference and Exhibition, EAGE. Extended Abstracts. https://doi.org/10.3997/2214-4609.201701153.
Vyas, M., Nichols, D., Mobley, E., 2011b. Efficient RTM angle gathers using source directions. In: 81th Annual International Meeting, SEG, Expanded Abstracts, pp. 3104–3108. https://doi.org/10.1190/1.3627840.
Wang, B.L., Gao, J.H., Chen, W.C., et al., 2013. Extracting efficiently angle gathers using Poynting vector during reverse time migration. Chin. J. Geophys. 56 (1), 262–268. https://doi.org/10.6038/cjg20130127.
Wang, N., Zhou, H., Chen, H., et al., 2018a. A constant fractional-order viscoelastic wave equation and its numerical simulation scheme. Geophysics 83 (1), T39–T48. https://doi.org/10.1190/geo2016-0609.1.
Wang, W., McMechan, G.A., Zhang, Q., 2015. Comparison of two algorithms for isotropic elastic P and S vector decomposition. Geophysics 80 (4), T147–T160. https://doi.org/10.1190/geo2014-0563.1.
Wang, Y.F., Zhou, H., Zhang, Q.C., et al., 2017a. Wavefield reconstruction in attenuating media using time-reversal checkpointing and k-space filtering. In: 79th Annual International Conference and Exhibition, EAGE. Extended Abstracts. https://doi.org/10.3997/2214-4609.201701152.
Wang, Y.F., Zhou, H., Zhao, X.Z., et al., 2017b. The k-space Green's functions for decoupled constant-Q wave equation and its adjoint equation. In: 79th Annual International Conference and Exhibition, EAGE. Extended Abstracts. https://doi.org/10.3997/2214-4609.201701153.
Wang, Y., Harris, J.M., Bai, M., et al., 2022. An explicit stabilization scheme for Q-compensated reverse time migration. Geophysics 87 (3), F25–F40. https://doi.org/10.1190/geo2021-0134.1.
Wang, Y., Zhou, H., Chen, H., et al., 2018b. Adaptive stabilization for Q-compensated reverse time migration. Geophysics 83 (1), S15–S32. https://doi.org/10.1190/geo2017-0244.1.
Wang, Y., Zhou, H., Zhao, X., et al., 2019. Q-compensated viscoelastic reverse time migration using mode-dependent adaptive stabilization scheme. Geophysics 84 (4), S301–S315. https://doi.org/10.1190/geo2018-0423.1.
Wu, B., Yang, H., Sun, W., et al., 2018. Common offset 3D prestack seismic data anti-aliasing beamforming, migration and imaging. Chin. J. Geophys. 61 (8), 3297–3309. https://doi.org/10.6038/cjg2018L0784.
Xiao, X., Leaney, W.S., 2010. Local vertical seismic profiling (VSP) elastic reverse-time migration and migration resolution: salt-flank imaging with transmitted P-to-S waves. Geophysics 75 (2), S35–S49. https://doi.org/10.1190/1.3309460.
Xie, Y., Sun, J., Zhang, Y., et al., 2015. Compensating for visco-acoustic effects in TTI reverse time migration. In: 85th Annual International Meeting, SEG, Expanded Abstracts, pp. 3996–4001. https://doi.org/10.1190/segam2015-5855445.1.
Xing, G., Zhu, T., 2019. Modeling frequency-independent Q viscoacoustic wave propagation in heterogeneous media. J. Geophys. Res. Solid Earth 124 (11), 11568–11584. https://doi.org/10.1029/2019JB017985.
Xu, S., Zhang, Y., Tang, B., 2011. 3D angle gathers from reverse time migration. Geophysics 76 (2), S77–S92. https://doi.org/10.1190/1.3536527.
Yan, J., Ross, W., 2013. Improving the stability of angle gather computation using Poynting vectors. In: 83th Annual International Meeting, SEG, Expanded Abstracts, pp. 3784–3788. https://doi.org/10.1190/segam2013-0632.1.
Yang, K., Wang, X., Zhang, J., 2022. Elastic reverse time migration angle gathers using a stabilized Poynting vector without zero points within the wave propagation ranges. Geophysics 87 (3), S137–S150. https://doi.org/10.1190/geo2021-0415.1.
Yang, P., Brossier, R., Métivier, L., et al., 2016. Wavefield reconstruction in attenuating media: a checkpointing-assisted reverse-forward simulation method. Geophysics 81 (6), R349–R362. https://doi.org/10.1190/geo2016-0082.1.
Yoon, K., Marfurt, K.J., 2006. Reverse-time migration using the Poynting vector. Explor. Geophys. 37 (1), 102–107. https://doi.org/10.1071/EG06102.
Yoon, K., 2017. Reverse time migration angle gathers using Poynting vector and pseudospectral method. In: 87th Annual International Meeting, SEG, Expanded Abstracts, pp. 4630–4634. https://doi.org/10.1190/segam2017-17749395.1.
Yoon, K., Guo, M., Cai, J., et al., 2011. 3D RTM angle gathers from source wave propagation direction and dip of reflector. In: 81th Annual International Meeting, SEG, Expanded Abstracts, pp. 1057–1060. https://doi.org/10.1190/1.3627847.
Yoon, K., Marfurt, K.J., Starr, W., 2004. Challenges in reverse-time migration. In: 74th Annual International Meeting, SEG, Expanded Abstracts, p. 1507. https://doi.org/10.1190/1.1851068, 1060.
Zhang, Q., 2014. RTM angle gathers and specular filter (SF) RTM using optical flow. In: 84th Annual International Meeting, SEG, Expanded Abstracts, pp. 3816–3820. https://doi.org/10.1190/segam2014-0792.1.
Zhang, Q., McMechan, G.A., 2011a. Common-image gathers in the incident phase-angle domain from reverse time migration in 2D elastic VTI media. Geophysics 76 (6), S197–S206. https://doi.org/10.1190/geo2011-0015.1.
Zhang, Q., McMechan, G.A., 2011b. Direct vector-field method to obtain angle-domain common-image gathers from isotropic acoustic and elastic reverse-time migration. Geophysics 76 (5), WB135–WB149. https://doi.org/10.1190/geo2010-0314.1.
Zhang, Q., McMechan, G.A., 2010. 2D and 3D elastic wavefield vector decomposition in the wavenumber domain for VTI media. Geophysics 75 (3), D13–D26. https://doi.org/10.1190/1.3431045.
Zhang, Q., McMechan, G.A., 2013. Polarization-based wave-equation migration velocity analysis in acoustic media. Geophysics 78 (6), U77–U88. https://doi.org/10.1190/geo2012-0428.1.
Zhang, Y., Liu, Y., Xu, S., 2020. Arbitrary-order Taylor series expansion-based

viscoacoustic wavefield simulation in 3D vertical transversely isotropic media. Geophys. Prospect. 68 (8), 2379–2399. https://doi.org/10.1111/1365-2478.12999.
Zhang, Y., Xu, S., Tang, B., et al., 2010. Angle gathers from reverse time migration. Lead. Edge 29 (11), 1364–1371. https://doi.org/10.1190/1.3517308.
Zhao, X., Zhou, H., Wang, Y., et al., 2018. A stable approach for Q-compensated viscoelastic reverse time migration using excitation amplitude imaging condition. Geophysics 83 (5), S459–S476. https://doi.org/10.1190/geo2018-0222.1.
Zhou, C., Jiao, J., Lin, S., et al., 2011. Multi-parameter joint tomography for anisotropic model building. In: 73rd Annual International Conference and Exhibition, EAGE. Extended Abstracts. https://doi.org/10.3997/2214-4609.20149473.
Zhu, H., 2017. Elastic wavefield separation based on the Helmholtz decomposition. Geophysics 82 (2), S173–S183. https://doi.org/10.1190/geo2016-0419.1.
Zhu, T., 2017. Numerical simulation of seismic wave propagation in viscoelastic-anisotropic media using frequency-independent Q wave equation. Geophysics 82 (4), WA1–WA10. https://doi.org/10.1190/geo2016-0635.1.
Zhu, T., Carcione, J.M., 2014. Theory and modelling of constant-Q P-and S-waves using fractional spatial derivatives. Geophys. J. Int. 196 (3), 1787–1795. https://doi.org/10.1093/gji/ggt483.
Zhu, T., Harris, J.M., 2014. Modeling acoustic wave propagation in heterogeneous attenuating media using decoupled fractional Laplacians. Geophysics 79 (3), T105–T116. https://doi.org/10.1190/geo2013-0245.1.
Zhu, T., Harris, J.M., Biondi, B., 2014. Q-compensated reverse-time migration. Geophysics 79 (3), S77–S87. https://doi.org/10.1190/geo2013-0344.1.